Supporting Information for

Weavable ion-electron hybrid gel fibers with adjustable thermopower and high output voltage for wearable energy harvesting

*Mao Zhang, Qianyang Li, Minhan Cheng, Jianwei Jing, Hua Deng**

College of Polymer Science and Engineering
State Key Laboratory of Advanced Polymer Materials
Sichuan University
Chengdu 610041, P. R. China
E-mail: huadeng@scu.edu.cn

1. Experimental section

Materials. Polyvinyl Alcohol (M_W=146000-186000, 99.3%-100% hydrolyzed) was purchased from Acros Organics. Methanol (AR, ≥ 99.5%), Sodium dodecylbenzene sulfonate(SDBS, ≥ 95.0%), sodium sulfate (Na_2SO_4, ≥ 99%), stearic acid (AR, ≥ 98.0%) and calcium chloride (AR, ≥ 96.0%) were obtained from Adamas. PEDOT:PSS was purchased from Heraeus, Germany. Single-walled carbon nanotubes (SWCNTs, NTP8022) were bought from Shenzhen Nanotech Port Co., Ltd., China. Ecoflex was provided by Smooth-On, America. Carbon black was purchased from Orion Engineers Carbons. Flax was provided by Yongsheng Cotton Weaving Factory. All reagents in this work were used without further purification.

Preparation of PEDOT:PSS/SWCNTs/PVA solution. The polyelectrolyte spinning solutions were prepared in the following way: firstly, 70 mg of SWCNTs and 23 mg of SDBS were added to 20 ml of deionized water, followed by ultrasonication at 200 W and 20 kHz in an ice bath with a 4-second on-off cycles for 40 minutes, resulting in a uniformly dispersed SWCNTs solution. Secondly, the aforementioned solution, PH1000 solution, and PVA were mixed and thoroughly stirred in a water bath at 90°C for 3 hours to obtain a homogeneous gel precursor solution. The resulting viscous solution was then centrifuged at 3000 rpm for 5 minutes to completely remove air bubbles.

Preparation of i-TE Hydrogel Fibers. Using a commercially available electric spinning machine, the precursor solution was extruded into a methanol coagulation bath at a rate of 5 ml $\min^{-1}$, and the spun long fibers were wound up at a speed of 18 rpm. The fibers underwent dehydration and phase transition in methanol. They were then immersed in Na_2SO_4 or $CaCl_2$ solutions of varying concentrations to introduce mobile ions. After soaking for 48 hours, stable p or n PPs i-TE hydrogel fibers were obtained.

Preparation of Ecoflex-coating encapsulated fibers. The fiber surface coating is primarily achieved through physical adsorption. First, the PPs hydrogel fiber is immersed in a dichloromethane solution containing 3 wt% stearic acid for 3 minutes, then withdrawn and dried in a fume hood for 5 minutes to evaporate the dichloromethane. During this process, the hydrophilic portion of the stearic acid interacts with the fiber surface, exposing the hydrophobic tails and forming a surface energy-matched hydrophobic barrier on the fiber. Subsequently, the fiber is placed in a 1:1 ratio-mixed, room-temperature curing Ecoflex premix solution and left at ambient temperature for 24 hours, thereby fabricating a stable Ecoflex-encapsulated PPs hydrogel fiber.

Preparation of the PPs fiber based i-TE device. The p/n i-TE fibers were cut into small segments of 1.5 cm in length. A mixed solution of carbon black and Ecoflex was used as the electrode to connect the fiber segments in a p-n alternating pattern, followed by coating with a layer of pure Ecoflex and curing at room temperature for 24 hours. Using flax as the substrate, the long composite gel fibers were sewn onto it, thus successfully fabricating a wearable fiber-based i-TE device.

Characterization. The determination of thermopower is performed using homemade equipment, including a Keithley voltmeter (2450) to record the voltage at both ends of the fiber, and a multi-channel temperature recorder (EX4000) connected to two thermocouples to record the temperature difference (ΔT) across the fiber. The ΔT is controlled by two Peltier modules regulated by a DC power supply. Unless otherwise specified, the test conditions are 25°C with 60% humidity. Electrical measurements are performed on the electrochemical ac impedance spectroscopy (EIS) using an electrochemical workstation (CHI660E, CH Instruments Ins, China), with the frequency range set from 10^{-1} to 10^5 Hz and the voltage amplitude of 10 mV. The ionic resistance (R_i) was obtained by extrapolating the low-frequency region of the Nyquist plot to the real impedance axis. The measurement is conducted along the fiber direction, and the conductivity is calculated using the following equation:

$$\sigma_i = \frac{l}{R_i \times S}$$

where S represents the effective electrode area, and l represents sample thickness. The moisture content (M) of the fiber is calculated using the following formula:

$$M = \frac{W_1 - W_2}{W_1} \times 100\%$$

The mechanical properties were measured using a universal tensile tester (WBE9000B) with a 10 N load cell. All samples were stretched at a rate of 20 mm min^{-1}. The resistance (R) was measured using a multimeter (Keithley, DMM7510). The measurement of sensitivity is conducted using a universal tensile testing machine combined with a multimeter. Additionally, the GF (Gauge Factor) is calculated according to the following equation:

$$GF = (\Delta R/R_0)/\varepsilon$$

where R_0 is the initial resistance, ΔR represents $R-R_0$ and ε represents the applied strain. The power density during the initial cycle was determined by attaching an external resistor. The current was monitored as the resistance was adjusted from 1 Ω to 10,000 Ω, and the output power was derived by squaring the current and multiplying it by the resistance. The zeta potential of the solution was evaluated at 25°C using dynamic light scattering (DLS, Brookhaven Zeta PALS 190 Plus). The thermal properties analysis was conducted through a thermogravimetric analyser (TGA, TG209 F1 Libra, NETZSCH, Germany). The infrared images were captured using an T620 infrared camera (FLIR Systems). FTIR tests of the samples were acquired using a Fourier transform infrared spectroscopy (Nicolet is50, FEI Corporation, USA) in the range of 4000-400 cm^{-1}. The morphologies of the freeze-dried fibers were sputtered with gold and characterized by field emission scanning electron microscopy (SEM, Apreo S HiVoc, FEI Corporation, USA). The conformational change of PEDOT and structure of SWCNTs was analyzed by Raman spectroscopy (LabRAM HR Evolution, HORIBA, Japan) using a 532 nm excitation wavelength.

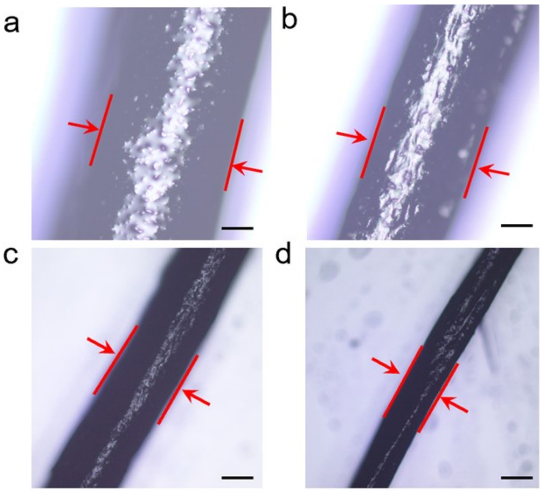

Fig. S1 Polarized optical microscope images of PPs fibers with diameter of (a) 0.9 mm, (b) 0.7 mm, (c) 0.4 mm and (d) 0.2 mm. Scale bars: 200 μm.

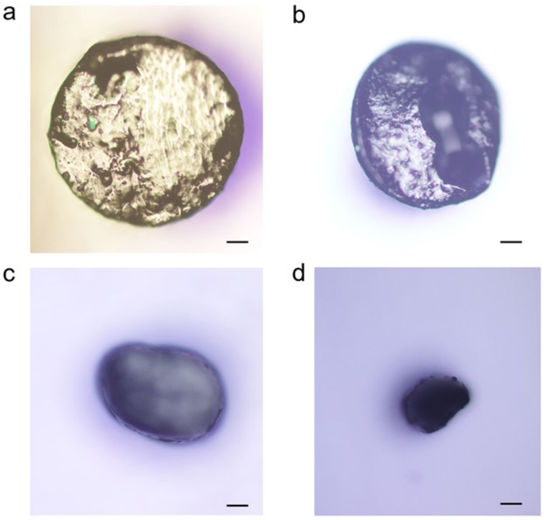

Fig. S2 Polarized optical microscope images of the cross-section of PPs fibers with diameter of (a) 0.9 mm, (b) 0.7 mm, (c) 0.4 mm and (d) 0.2 mm. Scale bars: 100 μm.

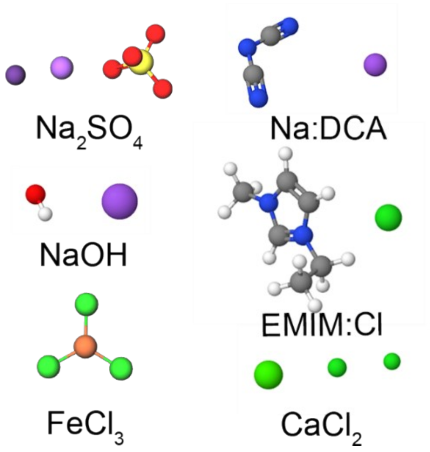

Fig. S3 The three-dimensional molecular structures of the selected ionic solutions for impregnating nascent fibers.

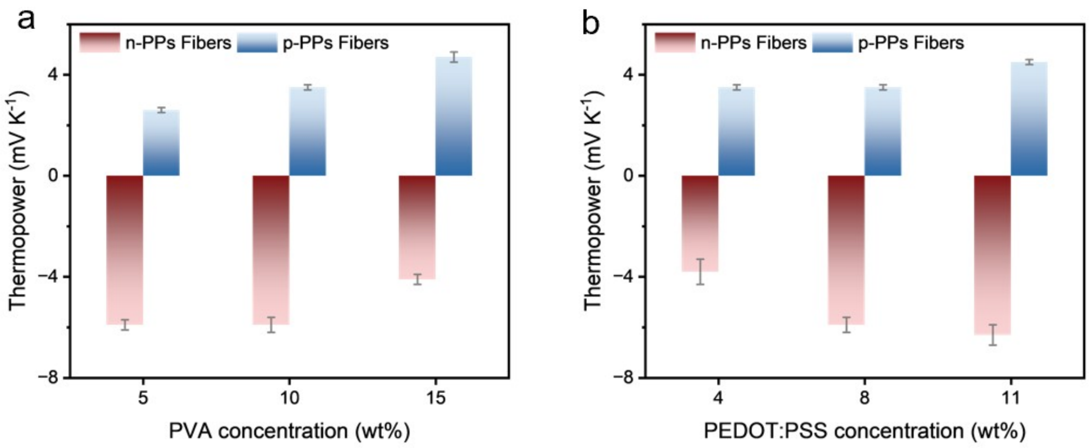

Fig. S4 The thermopowers of n&p-PPs fibers with different concentration of (a) PVA and (b) PEDOT:PSS.

The increase in the content of the non-conductive PVA matrix disrupts the electron transport pathways of SWCNT and PEDOT:PSS. When the content reaches 15 wt%, the disruption of electronic percolation channels in the fiber occurs. At this point, the charge density in the ionic channels is higher, and the migration resistance imposed on Cl^- and SO_4^{2-} increases. As a result, the thermopower of p-PPs gel fibers rises, while that of n-PPs gel fibers decreases. The thiophene rings in PEDOT:PSS provide an efficient pathway for electron transport, and increasing their content enhances electron conduction. However, a higher PSS content generates a Stern layer with elevated charge density, reducing the number of freely mobile ions in p-PPs.[1] In contrast, for n-PPs hydrogel fibers, Ca^{2+} only partially binds with PSS^- due to its higher charge density, leaving residual free Ca^{2+} and Cl^{-} available for conduction. This results in a continuous increase in σ_i. Additionally, owing to their small size and reduced electrostatic repulsion, Cl^{-} ions exhibit enhanced mobility, leading to an improvement in thermopower.

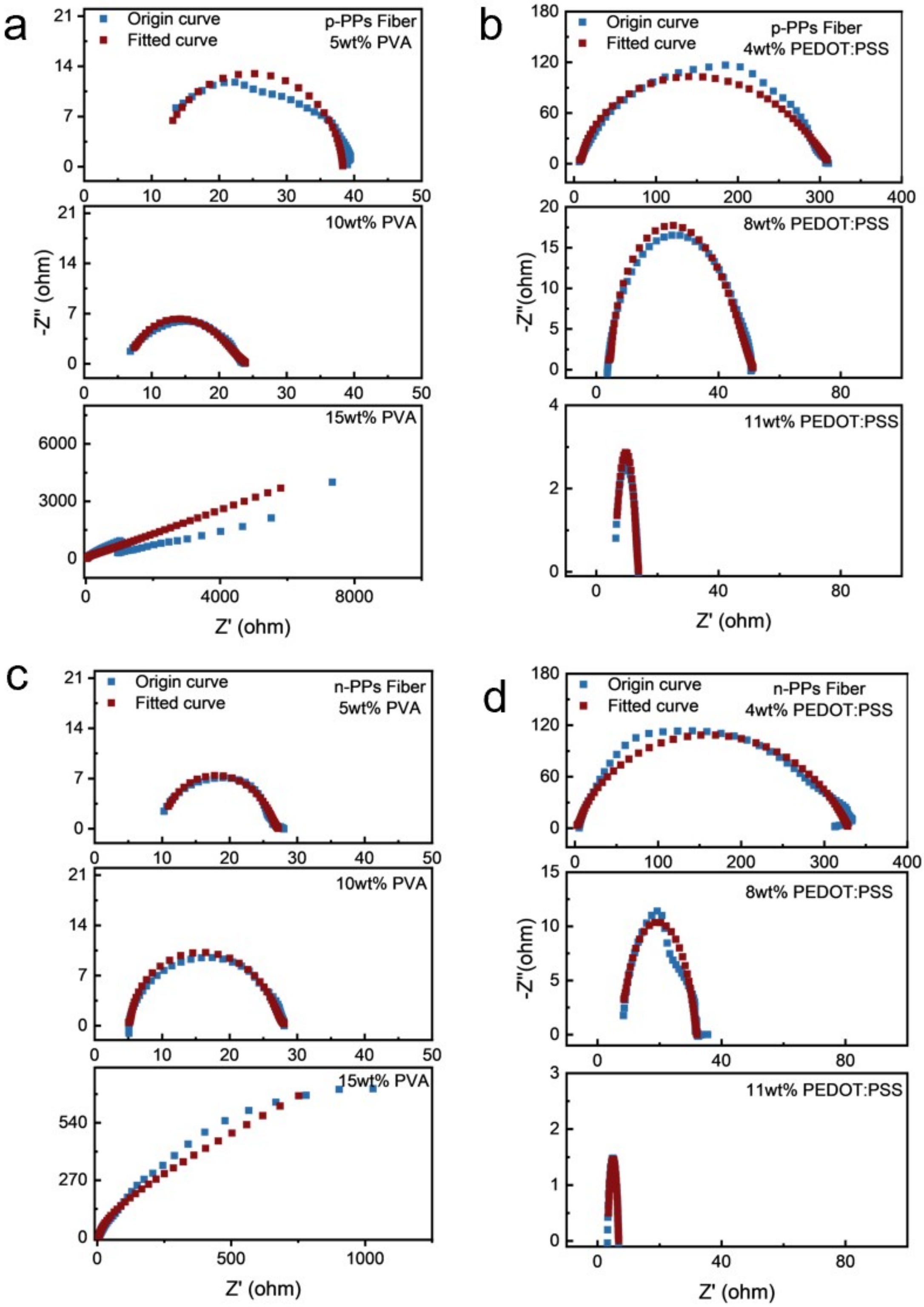

Fig. S5. The Nyquist plots and fitting curves of (a, c) p/n-PPs fiber with 5 wt%, 10 wt% and 15 wt% PVA. The Nyquist plots and fitting curves of (b, d) p/n-PPs fiber with 4 wt%, 8 wt% and 11 wt% PEDOT:PSS.

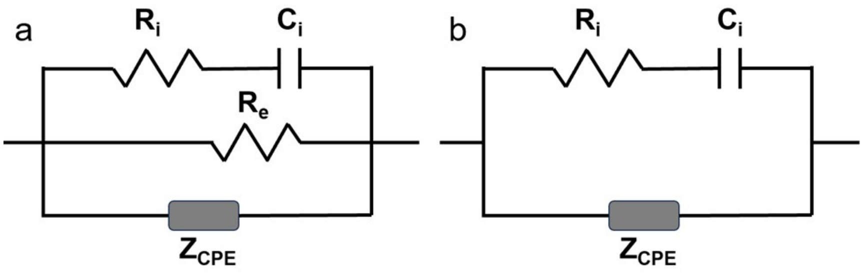

Fig. S6 The equivalent circuit of (a) mixed ionic-electronic conduction and (b) ion diffusion only.

When the Nyquist plot exhibits a semicircular shape, it indicates that the charge carrier transport within the fibers follows a mixed electron-ion conduction mechanism, and the corresponding equivalent circuit is shown in Fig S6a. Conversely, when the Nyquist plot displays a single sloping line, it signifies diffusion-dominated kinetics, and the equivalent circuit in this case is illustrated in Fig S6b.

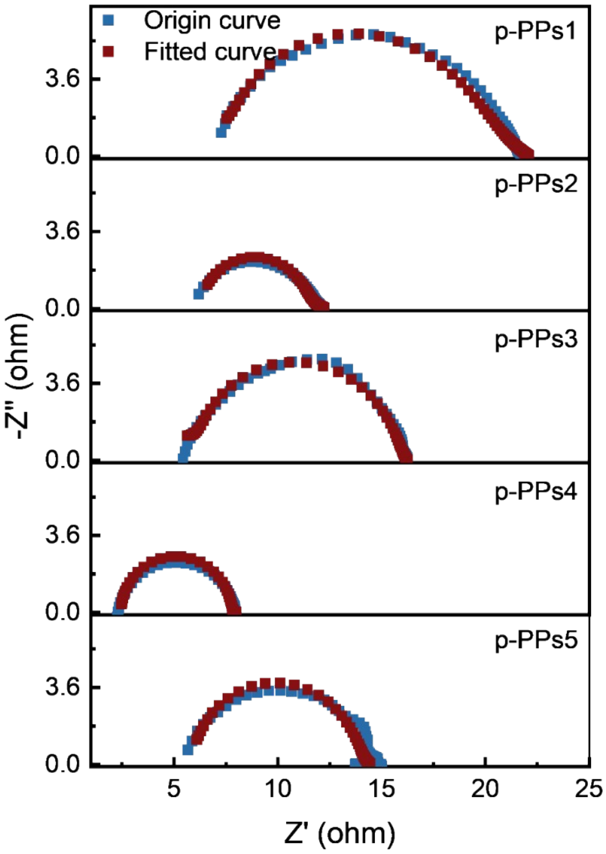

Fig. S7 The Nyquist plots and fitting curves of p-PPs1-5 hydrogel fibers.

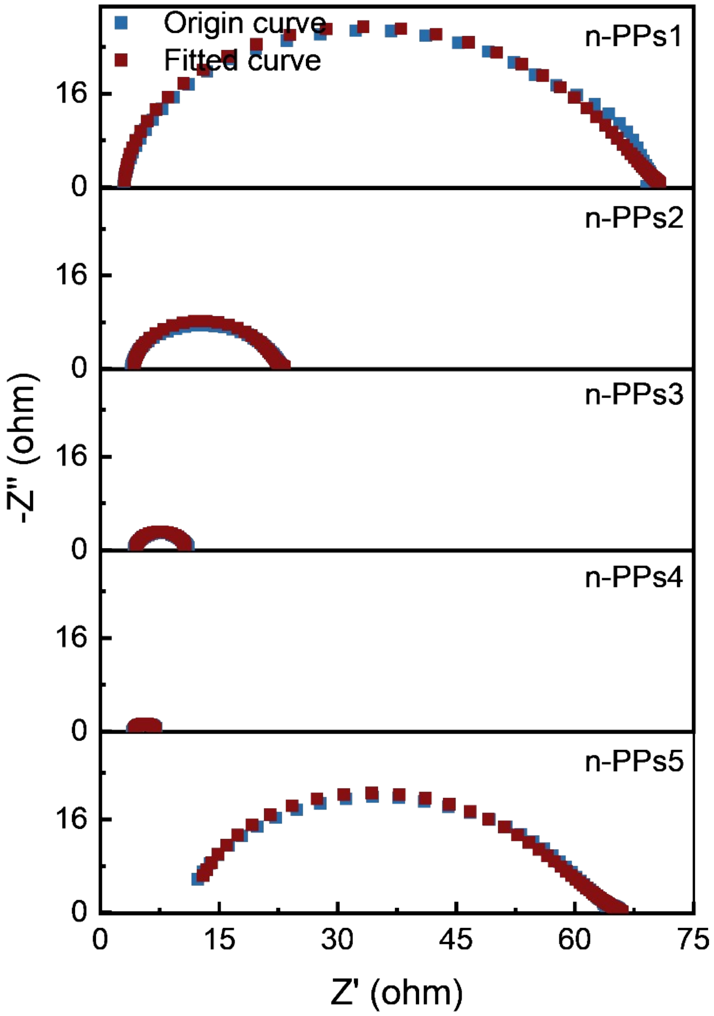

Fig. S8 The Nyquist plots and fitting curves of n-PPs1-5 hydrogel fibers.

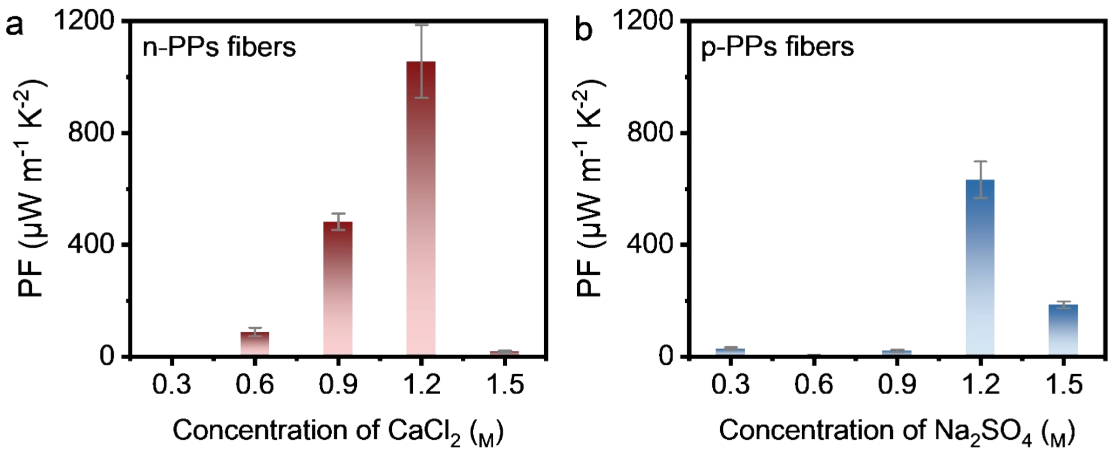

Fig. S9 The PF values of p&n-PPs fibers.

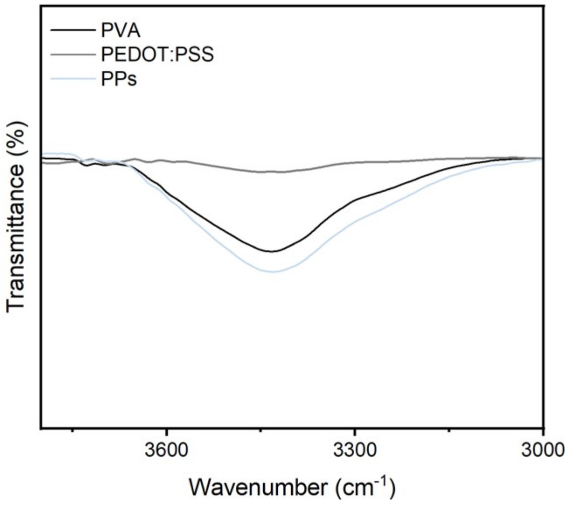

Fig. S10 The FTIR spectra of pure PVA, PEDOT:PSS and PVA/PEDOT:PSS/SWCNTs.

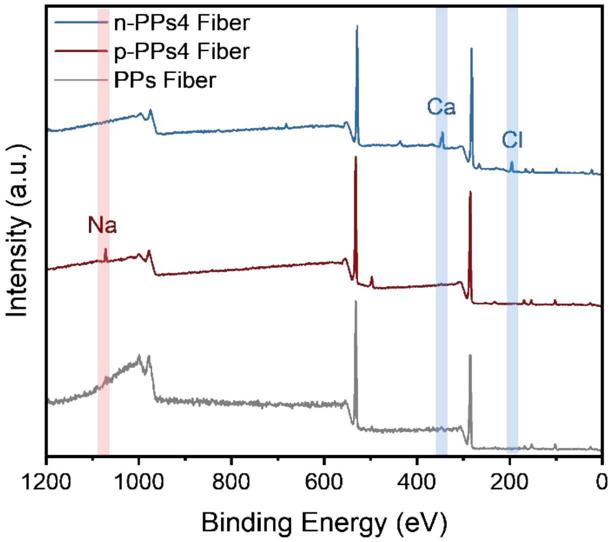

Fig. S11 Full X-ray photoelectron spectroscopy spectra of PPs, n-PPs4 and p-PPs4 hydrogel Fibers.

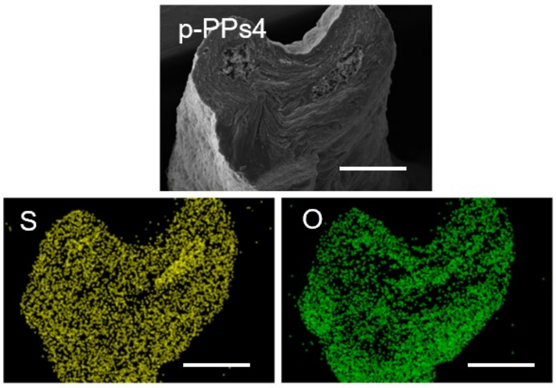

Fig. S12 The S and O elemental distribution of p-PPs4 hydrogel fiber mapped by EDS. Scale bars: 200 μm.

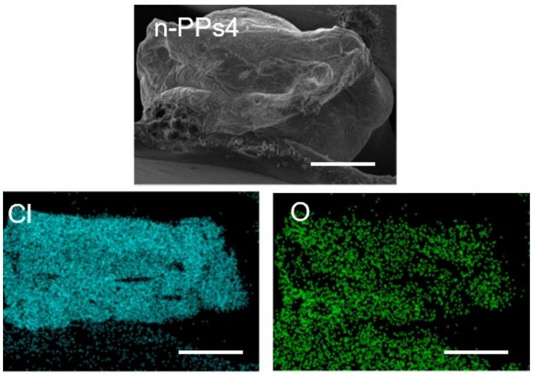

Fig. S13 The Cl and O elemental distribution of n-PPs4 hydrogel fiber mapped by EDS. Scale bars: 200 μm.

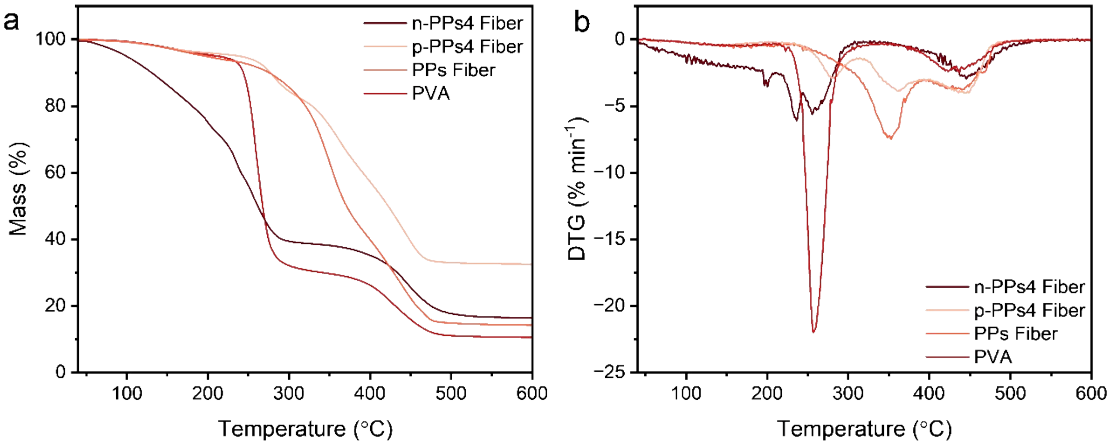

Fig. S14 (a) TG thermograms and (b) DTG curves of PVA, PPs, p-PPs4 and n-PPs4 hydrogel fibers.

The thermal stability of the gel fibers is influenced by compositional differences that alter internal interactions, as evidenced by the TG and DTG curves. In pure PVA, hydroxyl groups are progressively eliminated between 220.5°C and 318.1°C. The mass loss between 360.01°C and 496.74°C mainly results from backbone scission and degradation.[2] The dual-network PPs gel fiber incorporated with PEDOT:PSS and SWCNTs demonstrates enhanced thermal stability, exhibiting an elevated initial thermal decomposition temperature of 237.4°C. After treatment with 1.2_M $CaCl_2$ solution, the thermal stability decreases due to the disruption of intermolecular hydrogen bonding by the complexation of Ca^{2+} ions with -OH and $-SO_3H$ groups.[3] After treatment with Na_2SO_4, the physical crosslinked network restricts heat transfer, leading to a multi-step decomposition process.

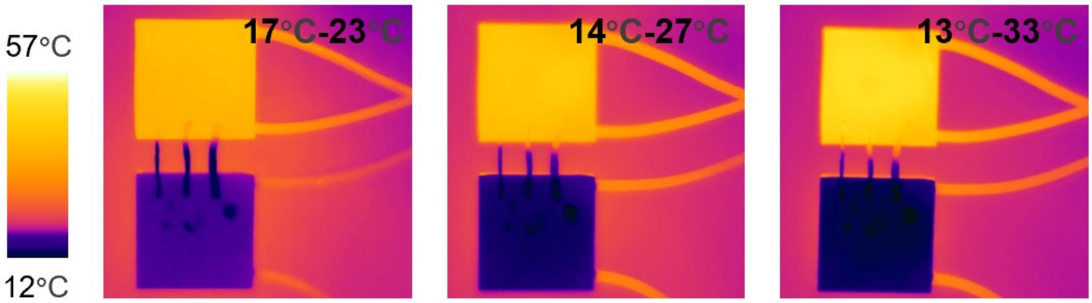

Fig. S15 Infrared camera images captured under varying temperature difference.

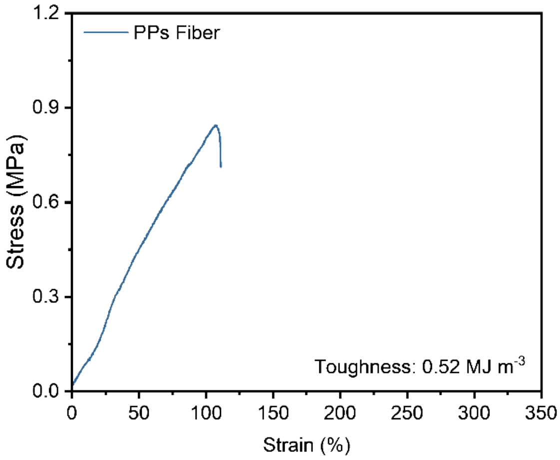

Fig. S16 Stress-strain curves of PPs hydrogel fibers with 2 wt% SWCNTs.

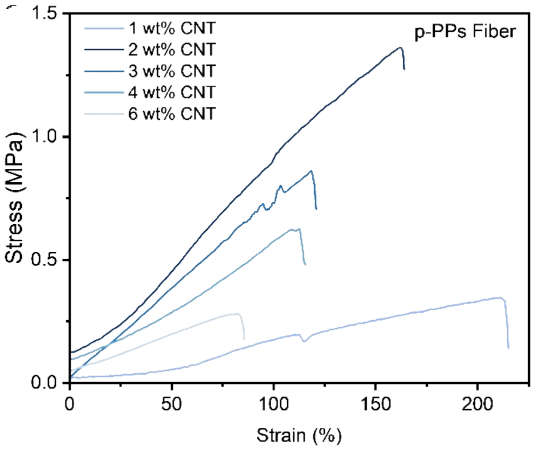

Fig. S17 Stress-strain curves of p-PPs hydrogel fibers with different contents of SWCNTs.

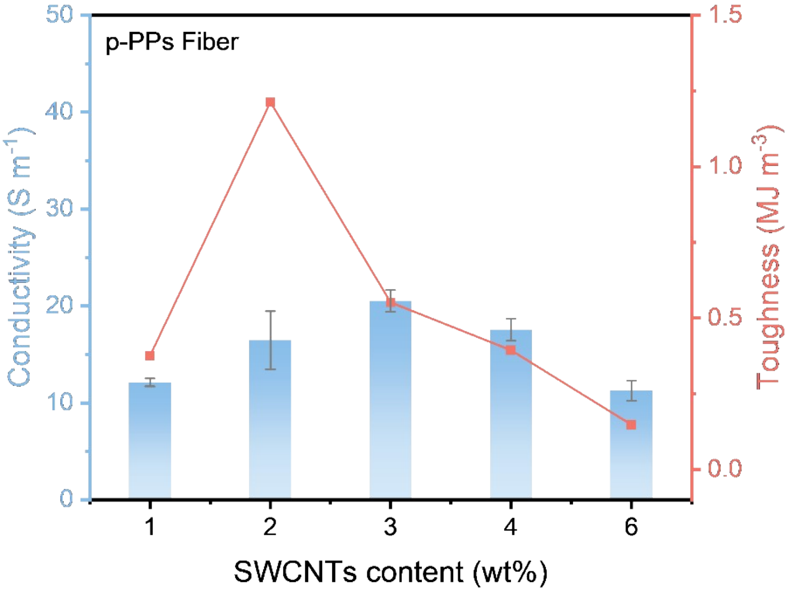

Fig. S18 Fracture strain and conductivity and of n-PPs hydrogel fibers with different SWCNTs contents.

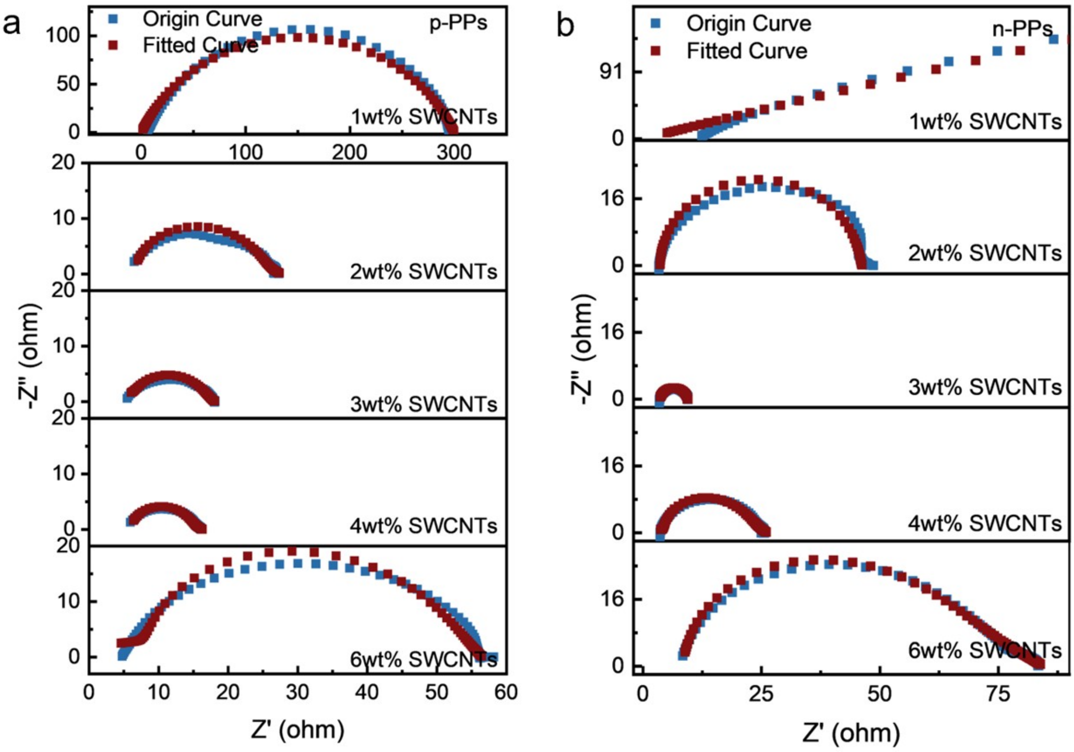

Fig. S19 The Nyquist plots and fitting curves of n&p-PPs hydrogel fibers with 1wt%, 2wt%, 3wt%, 4wt% and 6wt% SWCNTs.

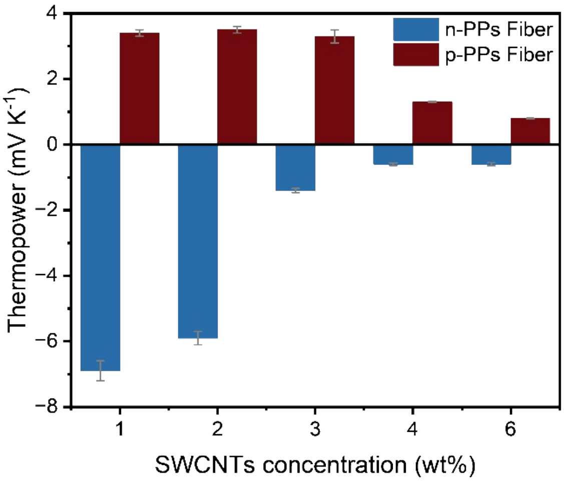

Fig. S20 Thermopowers of n&p-PPs hydrogel fibers with the concentrations of SWCNTs ranging from 1 wt% to 6 wt%.

The addition of electronically conductive fillers into i-TE systems essentially involves the competition and coupling of ion and electron transport, which can be discussed from the following perspectives:

a. The increase in conductivity ($\sigma = \sigma_i+\sigma_e$).

The incorporation of SWCNTs constructs an electron-conducting network within the PVA matrix. Under extreme conditions, as demonstrated in the study of Zhang et al. study, a PANa fiber containing 50 wt% SWCNTs achieved σ up to 200 S m^{-1}, while its Seebeck coefficient remained on the order of μV/K.[duibilizi3] In contrast, the PAM/LiTFSI composition, which contains only ionic components, exhibited a significantly high Seebeck coefficient of 19.02 mV K^{-1}, but its σ_i was only 2.5 S m^{-1}.[duibilizi2] The addition of SWCNTs significantly enhances the σ_e, but excessive incorporation can block ion transport pathways. In our work, with the coupling of ionic thermodiffusion, the σ reaches 51.6 S·m^{-1}.

b. The decrease in Seebeck coefficient (S)

When the SWCNTs content is below 4 wt%, the S remains at the mV K^{-1} level. However, when the content exceeds this threshold, it decreases rapidly due to two main reasons: First, after the formation of the highly conductive SWCNTs network, it rapidly counteracts the potential generated by ions during thermal diffusion.[1] Second, as the contribution of electronic conduction increases, the total thermopower shifts from being dominated primarily by the ionic component to approaching the electronic component. When the SWCNTs concentration exceeds 6 wt%, electronic transport becomes the dominant mechanism.

c. Change in stability

PVA, as a long-chain polymer, serves as both the structural material enabling wet-spinning and the ion-conducting matrix. SWCNTs enhance the mechanical strength, preventing gel deformation or fracture, while simultaneously improving σ. However, excessive SWCNT content causes agglomeration, resulting in fiber fracture. PEDOT:PSS acts as a bridge, coupling the electrical and mechanical properties of both the ionic and electronic components. The synergistic work of these three elements enhances both the TE functionality and mechanical stability of the gel.

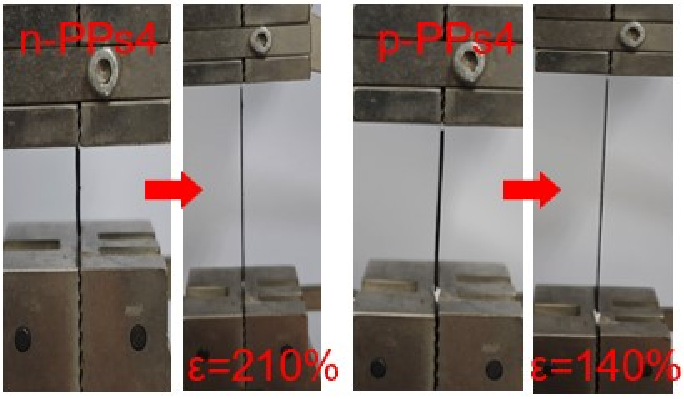

Fig. S21 Digital photographs of n-PPs4 hydrogel fiber in the initial and 210% strain loaded and p-PPs4 hydrogel fiber in the initial and 140% strain loaded.

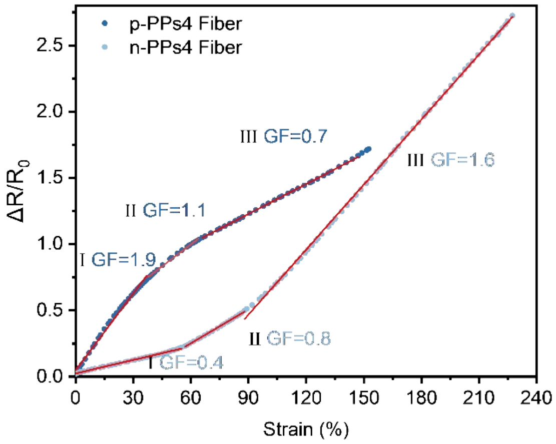

Fig. S22 Sensitivity of n&p-PPs4 fiber sensor.

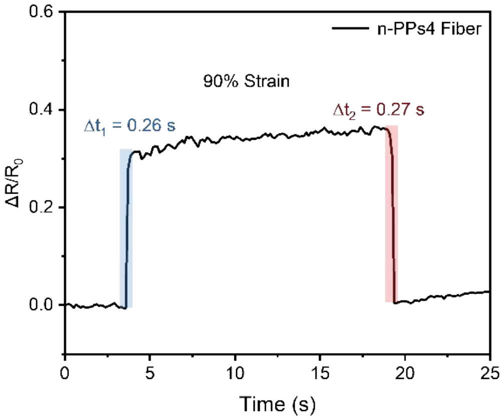

Fig. S23 Response and recovery time of the device assembled using n-PPs4 fibers.

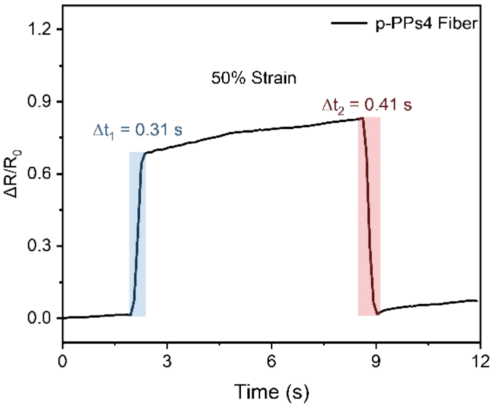

Fig. S24 Response and recovery time of the device assembled using p-PPs4 fibers.

The p-PPs-based flexible sensors exhibited response times of only 0.31 s during stretching and 0.41 s during recovery.

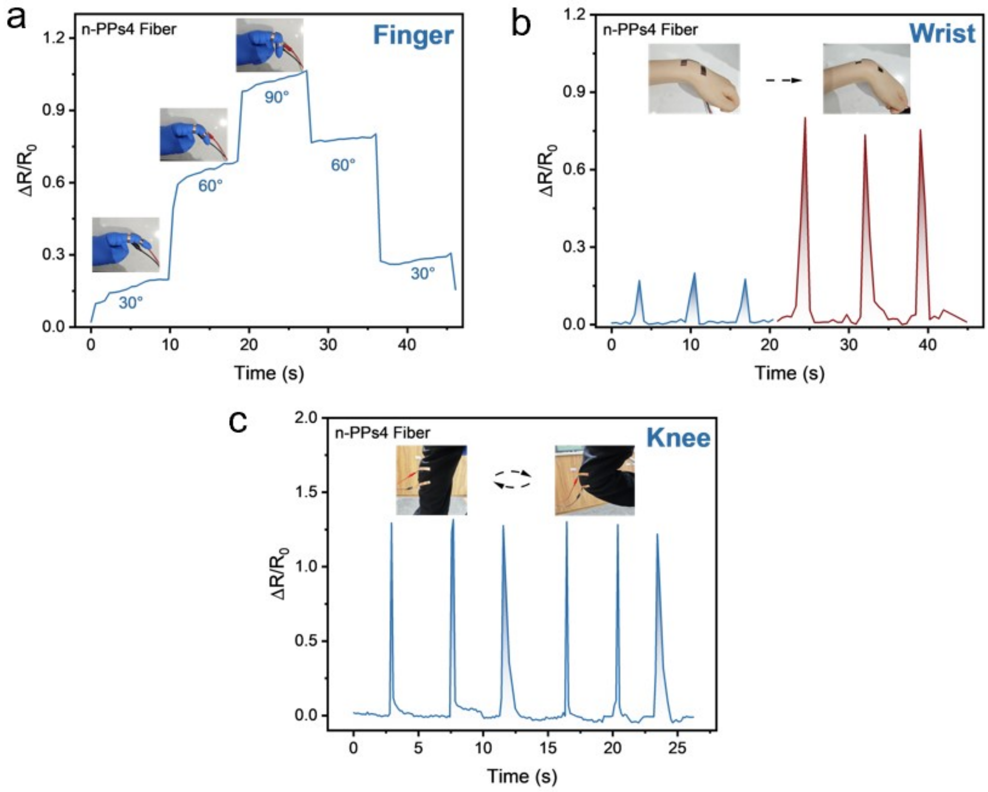

Fig. S25 Response and recovery time of the device assembled using n-PPs4 fibers. Signal monitoring of n-PPs4 hydrogel fiber sensors of resistance changes in (a) finger, (b) wrist and (c) knee.

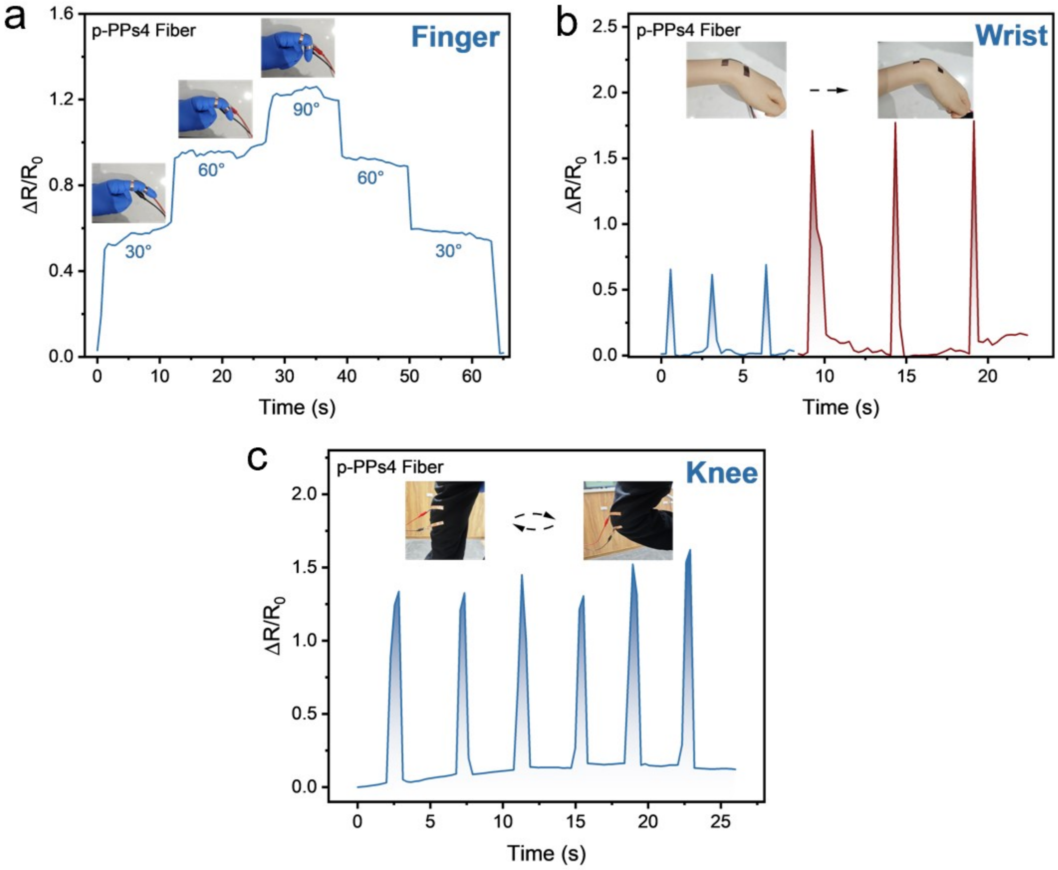

Fig. S26 Monitoring of resistance changes of the device assembled using p-PPs4 fibers in a) finger, b) wrist and c) knee.

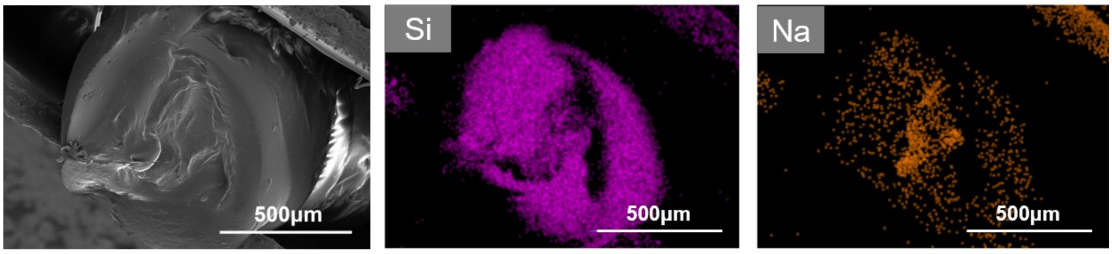

Fig. S27 SEM image, silicon element and sodium element distribution of the Ecoflex encapsulated p-PPs4 fiber.

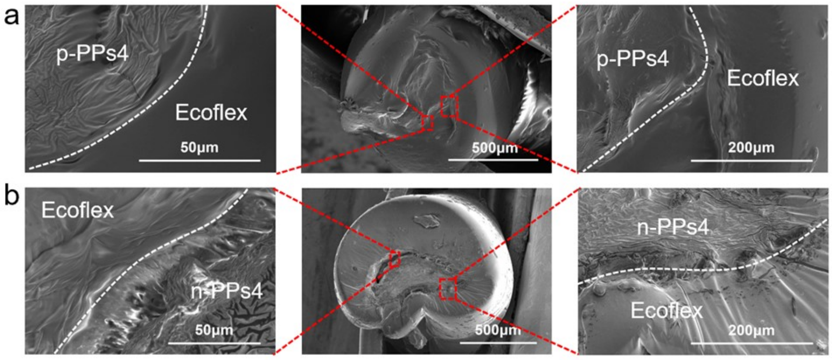

Fig. S28 SEM images of the Ecoflex layer-fiber interface for (a) p-PPs and (b) n-PPs fibers.

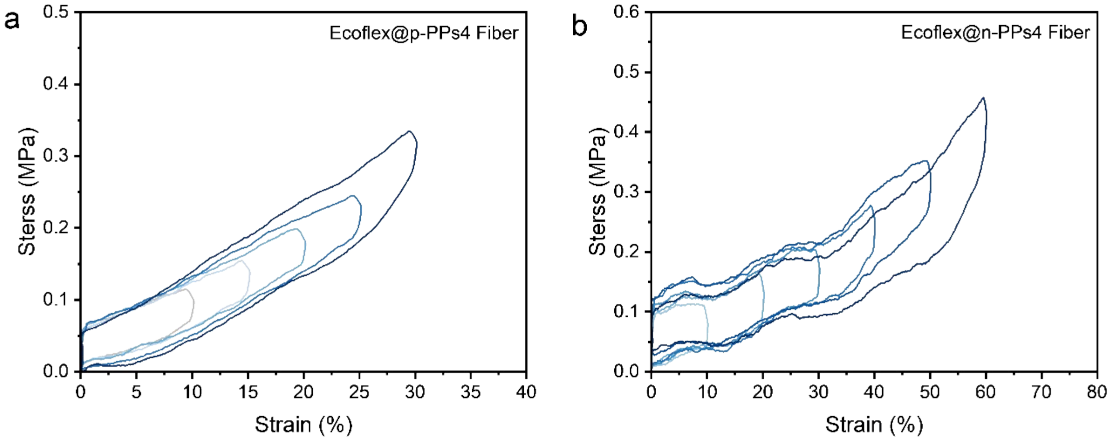

Fig. S29 Loading-unloading curves of (a) Ecoflex@p-PPs4 fiber within the strain range of 10-30 % with a 5 % strain increment and (b) Ecoflex@n-PPs4 fiber hydrogel fibers within the strain range of 10-60 % with a 10 % strain increment.

The stress recovery capability of polymer materials is a key measure of their mechanical performance. By subjecting the Ecoflex-coated fibers to multi-strain cyclic loading-unloading extension tests, we observed hysteresis loops caused by the disruption of physical cross-links or chain slippage, which exhibit both elastic recovery and energy dissipation capabilities. In addition, Ecoflex@n-PPs4 fiber demonstrates reversible recovery at 60% strain, exhibiting superior elasticity.

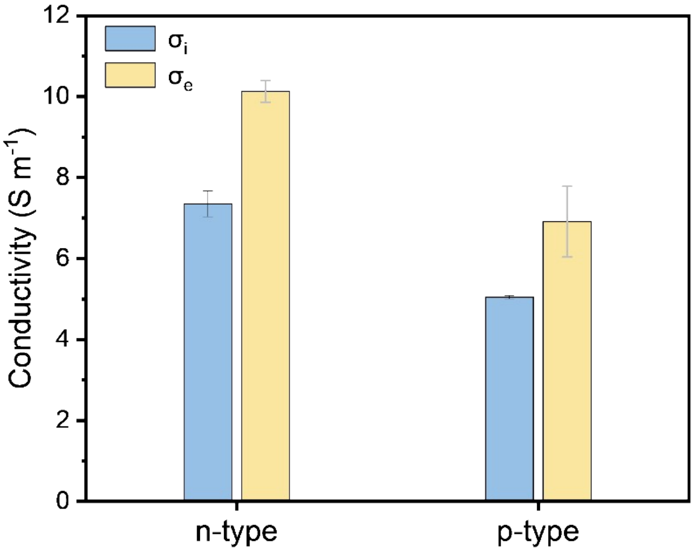

Fig. S30 Conductivity of Ecofilex@n-PPs4 hydrogel fiber and Ecofilex@p-PPs4 hydrogel fiber.

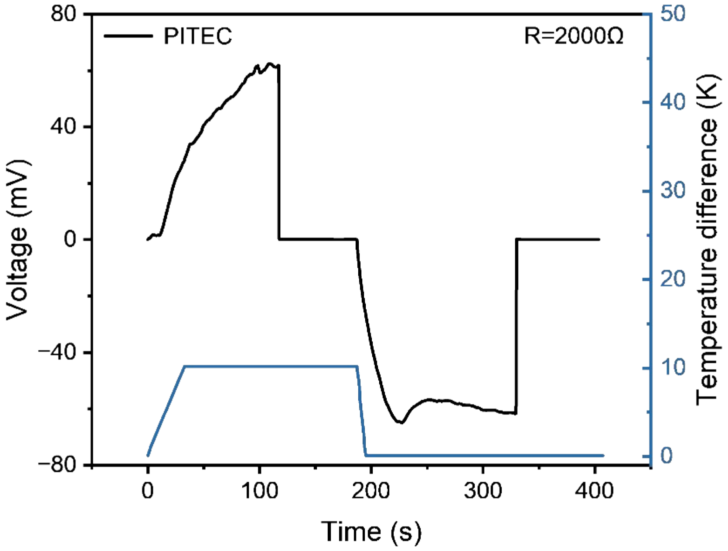

Fig. S31 Voltage and temperature gradient curves of the ITEC made of PITEC with an external load of 2 kΩ.

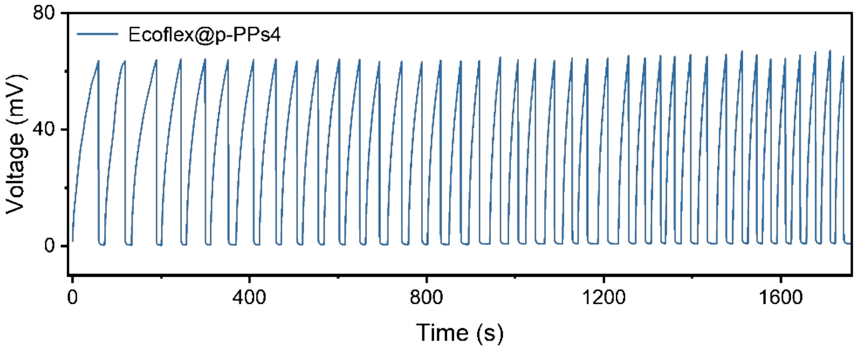

Fig. S32 Output voltage curve of the ITEC made of Ecoflex@p-PPs4 fiber over 40 cycles.

Fig. S31 gives the four-stage curve of the Ecoflex@p-PPs4 fiber based i-TE capacitor (PITEC). In Stage I, ΔT induced ionic diffusion polarization generates a thermovoltage of 62.4 mV under ΔT=8.2 K. During Stage II, this voltage is compensated by external electrons when connected to a 2 kΩ external load. Stage III begins with the removal of both the ΔT and external load, where ions drift back to their original positions while electrons and holes remain at the electrodes, creating a reverse voltage. In Stage IV, this compensation voltage gradually decays upon reconnection of the load, thereby completing the voltage conversion and utilization cycle. Notably, the NITEC demonstrates exceptional device stability over 40 charge-discharge cycles in Fig. S32, showing no significant performance degradation.

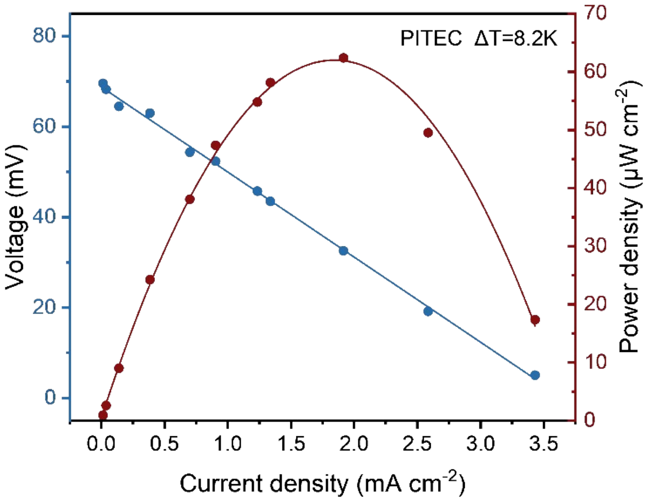

Fig. S33 Power density and thermovoltage of the first charging-discharging cycle of PITEC.

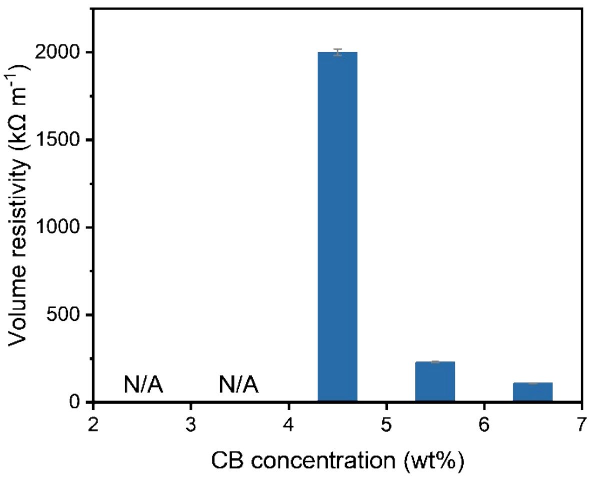

Fig. S34 The volume resistivity of elastic electrodes doped with varying amounts of carbon black.

Fig. S35 Optical images of the i-TE fabric with 24 p-n pairs.

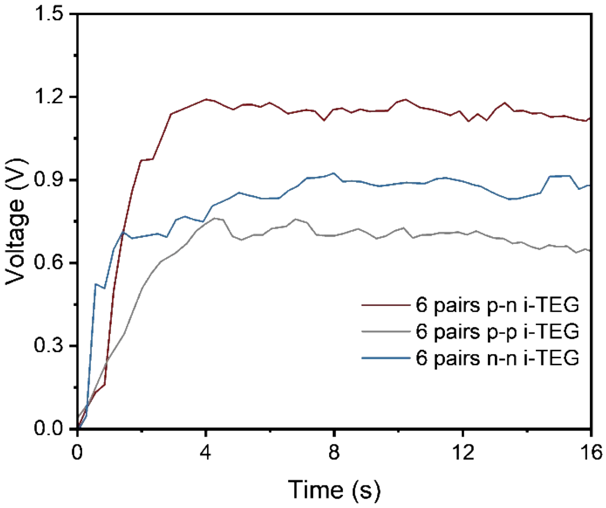

Fig. S36 The voltage output of i-TEG with 12 p-type units, 12 n-type units and 6 pairs of p-n junctions.

Fig. S37 Photo for the i-TE fabric with 6 p-n pairs worn on the arm.

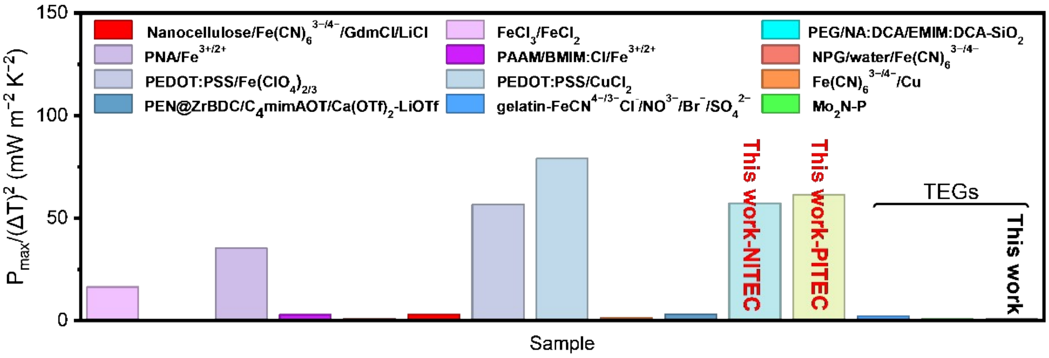

Fig. S38 The normalized maximum power density ($P_{max}/\Delta T^2$) comparison of the state-of-the-art literature data. (TEGs are defined as devices containing **more than one** TE component.)

The TEG module composed of 24 p-n legs shows a maximum current density of 2.85 μA m^{-2} and a $P_{max}/(\Delta T)^2$ of 0.3 mW m^{-2} K^{-2}. For a single-element device, the $P_{max}/(\Delta T)^2$ of NITEC over one thermal cycle is 57.2 mW m^{-2} K^{-2}, while that of PITEC is 61.4 mW m^{-2} K^{-2}. We have conducted a detailed comparison of this parameter with the latest state-of-the-art reported results, as outlined below in **Fig. S38.**[4-15] For the TEG fabricated with a single element, our developed material surpasses the majority of reported TE devices. However, it must be acknowledged that after fabricating a TEG with multiple elements connected in series, non-ideal electrode connections result in significant internal resistance.

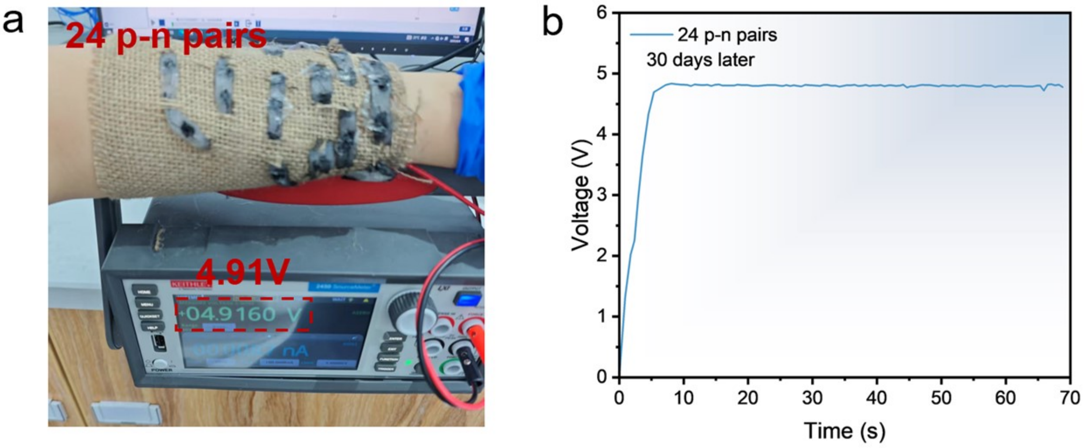

Fig. S39 (a) Photo and (b) voltage curve of the i-TE fabric with 24 p-n pairs worn on the arm after being placed in the atmospheric environment for 30 days.

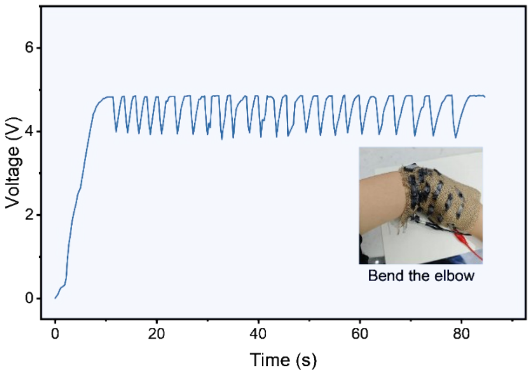

Fig. S40 Self-powered sensor curve for monitoring identical elbow flexion angles.

References

1. B. Yao, S. Wu, R. Wang, Y. Yan, A. Cardenas, D. Wu, Y. Alsaid, W. Wu, X. Zhu and X. He, *Adv. Funct. Mater.*, 2021, **32**, 2109506.
2. H. Xiao, M. Deng, C. Zhou, X. He and P. Yang, *Separation and Purification Technology*, 2025, **359**, 130571.
3. P. Singh, D. C. Bharati, P. N. Gupta and A. L. Saroj, *Journal of Non-Crystalline*

Solids, 2018, **494**, 21-30.

4. Z. Liu, Z. Li, M. Qu, H. Yang, J. Tang, F. Zhong, X. Wei, Y. Song, Z. Liu and H. Chen, *Chem. Eng. J.*, 2025, **523**, 168815.
5. L. Yang, J. Chen, C.-G. Han, Y. Zhu, C. Xie, Z. Liu, H. Wang, Y. Bao, D. Han and L. Niu, *Energy & Environmental Science*, 2025, **18**, 2559-2569.
6. L. Zhao, Y. Zhang, W. Zhou, X. Feng and J. Ouyang, *Small*, 2025, **21**, 2503338.
7. X. Shi, Y. Li, N. Shi, C. Ji, L. Hou, Y. Shi, J. Xu, Y. Lan, Q. Wei, G. Ma, P. Wu and Z. Hu, *Nat. Commun.*, 2025, **16**, 9002.
8. W. Tai, J. Jia, W. Zhang, Y. Dai, Q. Wang and W. Zeng, *Chem. Eng. J.*, 2025, **509**, 161288.
9. Y. Xu, Z. Li, S. Li, Y. Xu and X. Zhang, *Adv. Funct. Mater.*, 2025, **e13969**.
10. B. Xie, Z. Chen, H. Li, Z. Liu, M. Li, Y. Huang, G. Chen and Z. Liu, *Adv. Funct. Mater.*, 2025, **e19934**.
11. J. X. Gui, Y. Cheng, K. Ren, Z. P. Liu, Z. Zhu, Z. Y. Xue, Y. Zhu, R. H. Wang, G. Pei, J. Sui and L. F. Chen, *Adv. Mater.*, 2025, **37**, 2420214.
12. J.-Y. Baek, H. J. Seog and S.-Y. Jang, *Energy & Environmental Science*, 2025, **18**, 6714-6721.
13. D. H. Kim, B. Kim, J. Y. Baek, H. J. Seog and S. Y. Jang, *Adv. Funct. Mater.*, 2025, **e14954**.
14. X. He, H. Sun, P. Yu, H. Li, Z. Zhang, Y. Niu, J. Jiang and C. Wang, *Adv. Energy Mater.*, 2025, **e02570**.
15. Z. Hu, C. Sun and Y. Xuan, *Adv. Mater.*, 2025, **37**, 2419477.